Temperature dependence of Eu-related EPR spectra in CsBr:Eu needle image plates

F. Loncke, H. Vrielinck, P. Matthys, and F. Callens
Department of Solid State Sciences, Ghent University, Krijgslaan 281-S1, B-9000 Gent, Belgium

J.-P. Tahon and P. Leblans
Agfa Healthcare NV, Septestraat 27, B-2640 Mortsel, Belgium

I. Ahmad and E. Goovaerts
Department of Physics, University of Antwerp, Universiteitsplein 1, B-2610 Antwerpen (Wilrijk), Belgium
(Received 21 January 2009; published 1 May 2009)

Vacuum-deposited CsBr needle plates doped with Eu^{2+} have been investigated with Q (~34 GHz) and W (~95 GHz) band electron paramagnetic resonance in a large temperature interval (4 K: room temperature). At low temperatures (<35 K), two Eu-related centers were found with different symmetry (tetragonal and orthorhombic), while in earlier studies at room temperature only one center was found with tetragonal symmetry. Possible models for the three defects are investigated, taking into account their temperature behavior, their symmetry, and the atypical values of their zero-field splitting parameters.

DOI: 10.1103/PhysRevB.79.174102 PACS number(s): 61.72.Hh, 87.59.bd, 71.20.Eh

I. INTRODUCTION

In radiography, digital image plates based on x-ray storage phosphors are in many hospitals rapidly replacing the conventional screen/film technology. X-ray irradiation produces room-temperature (RT) stable defects in the phosphor (trapping of electrons and holes) that store the image. This image can be read out via photostimulated luminescence (PSL). The trapped charge carriers are released to recombine via emission of light, the intensity of which is detected in order to construct the digital image.[1] The commercial $BaFBr:Eu^{2+}$ powder-based image plates suffer from a loss of resolution due to light scattering. Various other compounds (CsBr, RbBr, etc.), on the other hand, can be grown in needle image plates (NIPs). These are thermal vapor-deposited binderless screens, consisting of needle-shaped microcrystals, oriented perpendicular to the plane of the plate. Using NIPs strongly reduces the resolution problem and since $CsBr:Eu^{2+}$ has several other favorable x-ray storage properties (high x-ray absorption, high conversion efficiency, low read-out energy, easy erasability, etc.),[2] the rapidly growing appearance in hospitals of $CsBr:Eu^{2+}$ based NIPs is not surprising. Up until now, however, the physics of the writing (storage) and read-out process in these plates are not well understood, unlike for the $BaFBr:Eu^{2+}$-based powder plates, where the electron paramagnetic resonance (EPR) played a major role in identifying the key defects involved.[3]

We recently reported the results of a first Q band (~34 GHz) EPR study on NIPs at RT.[4] A strong EPR signal labeled AA-EPR was detected, in contrast with as-grown Bridgman $CsBr:Eu^{2+}$ single crystals, where no EPR signal could be found (Ref. 5 and own results). The analysis showed that the signal was due to a tetragonal Eu^{2+}-related defect, with its symmetry axis along one of the crystal ⟨100⟩ axes. The values of the EPR parameters of this defect are reproduced in Table I. Furthermore, measuring both the EPR signal before irradiation and the PSL yield after irradiation on different NIPs revealed the linear correlation between EPR and PSL signal intensity,[6] which strongly suggests that this paramagnetic Eu-related defect plays a direct role in the storage (e.g., as a hole trap) and/or read-out (e.g., as the PSL active emission center) process of the image plate. Electron nuclear double-resonance (ENDOR) measurements are the next step to obtain more information about the precise nature of this defect, as they can identify and localize the surrounding nuclei. Lowering the temperature (T) to saturate the EPR signal was found to lead to a drastic change in the EPR spectrum. This change cannot be explained by a mere tem-

TABLE I. EPR parameters for the different Eu-related centers.

AA-EPR I (4 K)	
g	1.991_4
$\mathbf{B}_2^0$ (MHz)	$-964.6_{6.9}$
$\mathbf{B}_4^0$ (MHz)	-0.27_{10}
$\mathbf{B}_4^4$ (MHz)	4.77_{65}
AA-EPR II (4 K)	
g	1.993_3
$\mathbf{B}_2^0$ (MHz)	$815.6_{9.1}$
$\mathbf{B}_2^2$ (MHz)	778_{21}
$\mathbf{B}_4^0$ (MHz)	0.59_{14}
$\mathbf{B}_4^2$ (MHz)	$-1.7_{1.2}$
$\mathbf{B}_4^4$ (MHz)	$-2.2_{1.2}$
AA-EPR(RT)[a]	
g	1.991_5
$\mathbf{B}_2^0$ (MHz)	-755_{11}
$\mathbf{B}_4^0$ (MHz)	-0.27_{18}
$\mathbf{B}_4^4$ (MHz)	3.47_{99}

[a]Values taken from Ref. 4, signs adapted to match with AA-EPR I.

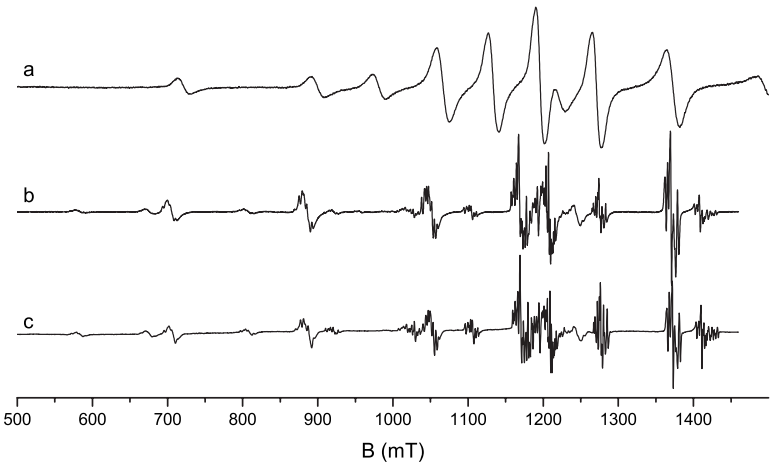

FIG. 1. Normalized Q band spectra with the magnetic field perpendicular to the plate (i.e., the $\langle 100 \rangle$ spectrum) of a 1-mm-thick CsBr:Eu^{2+} NIP produced at Agfa Healthcare at (a) RT and at (b) 4 K and of a commercial plate (Hamamatsu A0 605490) at (c) 4 K.

perature dependence of the zero-field splitting (ZFS) parameters.

In this work, we present a consistent analysis of the Q and W ($\sim$95 GHz) band spectra of both powdered NIPs and intact plate material at low temperature (LT). We also discuss the temperature behavior of the spectrum in relation to possible defect models.

II. EXPERIMENTAL AND METHODS

A 1-mm-thick CsBr:Eu^{2+} NIP was prepared via thermal vapor deposition at Agfa Healthcare NV and optimized for PSL activity. Eu^{2+} was incorporated via Eu-containing salts to a concentration of about 500 ppm. For comparison, experiments have also been performed on a commercial plate from Hamamatsu (A0 605490). X-ray diffraction (XRD) measurements revealed that the long axis of the needles corresponds to a $\langle 100 \rangle$ crystal axis, so that a single-crystal-like $\langle 100 \rangle$ spectrum can be recorded when the external magnetic field is perpendicular to the plate (or parallel to the needle axes), in a similar way as explained in our RT study.[4] Depending on the evaporation parameters, a certain level of in-plane orientation of the needles is found. In Ref. 4 we used the term "two-dimensional (2D) powder" to describe the spectrum with the magnetic field parallel to the plate, since only orientations perpendicular to $\langle 100 \rangle$ (e.g., a [111] crystal axis cannot occur in this plane) are present. In the ideal situation for a plate wherein no preferential in-plane orientation occurs, all orientations within this plane equally contribute to the EPR spectrum, leaving only the transitions at extremal resonance fields observable in the angular dependence.

Rectangular pieces ($\sim 1.4 \times 10$ mm^2) were carefully cut from the plates with a cleaving knife and positioned in a standard EPR (clear-fused quartz) tube with the plane of the plate parallel to the axis of the sample tube. To record powder spectra, pieces of NIPs were crushed in a mortar and an EPR tube was filled to a height of typically 1 cm.

Q band EPR and ENDOR spectra and W band EPR spectra were recorded on a Bruker ElexSys E500 and a Bruker ElexSys E680 spectrometer, respectively. Both are equipped with a continuous flow helium cryostat ($\sim$3–300 K). In the Q band setup, the maximum magnetic field is 1.5 T, while with the W band spectrometer equipped with a superconducting magnet fields up to 5.5 T can be attained.

The spectra were analyzed and simulated (including temperature effects) using EASYSPIN.[7] Eu^{2+} has a $[Xe]4f^7$ configuration, resulting in an $^8S_{7/2}$ ground state and an electronic spin $S=7/2$. The EPR spectra were analyzed using the following spin Hamiltonian:

$$\hat{\mathbf{H}} = \beta_e \vec{\mathbf{B}} \cdot \vec{\mathbf{g}} \cdot \hat{\vec{\mathbf{S}}} + \hat{\mathbf{H}}_{\mathbf{ZFS}},$$

where all interactions with (neighboring) nuclei are neglected. In the ZFS Hamiltonian,

$$\hat{\mathbf{H}}_{\mathbf{ZFS}} = \sum_{\mathbf{k}} \sum_{\mathbf{q} \le \mathbf{k}} \mathbf{B}_{\mathbf{k}}^{\mathbf{q}} \hat{\mathbf{O}}_{\mathbf{k}}^{\mathbf{q}},$$

$\hat{\mathbf{O}}_{\mathbf{k}}^{\mathbf{q}} = \hat{\mathbf{O}}_{\mathbf{k}}^{\mathbf{q}}(\hat{\mathbf{S}}_{\mathbf{x}}, \hat{\mathbf{S}}_{\mathbf{y}}, \hat{\mathbf{S}}_{\mathbf{z}})$ represent the extended Stevens operators[7,8] and $k=2$, 4, and 6 since $k \le 2S$. Due to the large linewidths observed in our spectra (see Figs. 1–5), the fitting of the spectra could not be significantly improved by the introduction of anisotropy in the g tensor or nonzero $\mathbf{B}_6^{\mathbf{q}}$ parameters, which were not further considered.

Finally, x-ray irradiations at RT were performed using a Philips x-ray tube operated at 60 kV and 40 mA in order to check the resistance to radiation damage of the paramagnetic centers present before irradiation.

III. RESULTS

A. $\langle 100 \rangle$ spectrum at 4K

When cooling the sample from RT to liquid He temperature, the EPR spectrum undergoes a dramatic change. In Fig. 1 the $\langle 100 \rangle$ Q band EPR spectrum at RT and at 4 K is shown. When comparing both spectra, the similar field range and the size of the line splittings suggest that they originate from the same type of center, i.e., Eu^{2+}, as will be further substantiated below. On the other hand, it is clear that these spectra exhibit several differences which complicate finding the link between them; for example, at 4 K the number of lines is larger than at RT and a complex hyperfine (HF) or superhyperfine (SHF) structure is visible on several transitions. Analyzing this structure from the EPR spectra alone is not obvious. In Fig. 1(c), the $\langle 100 \rangle$ spectrum at 4 K is shown for a

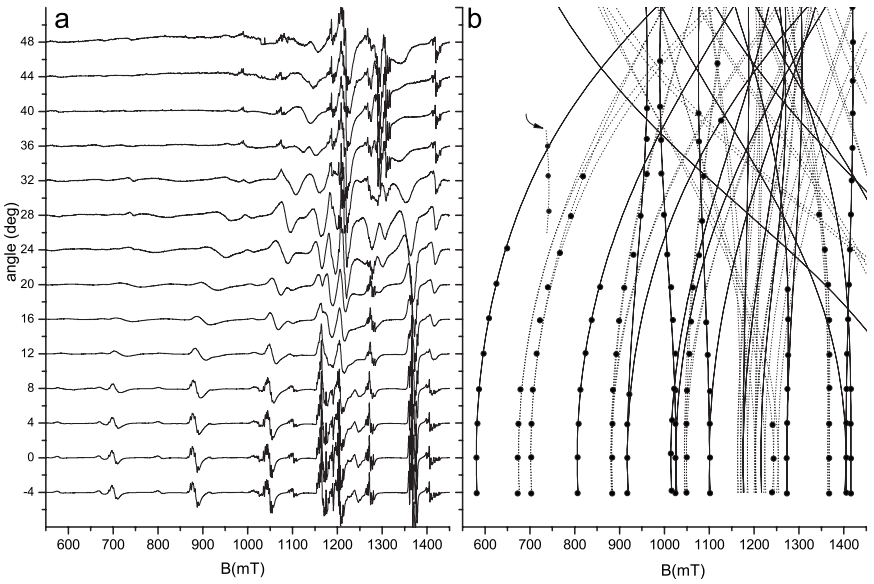

FIG. 2. (a) 4 K *Q* band angular variation with the magnetic field rotated in a plane perpendicular to the plate, at 0° the ⟨100⟩ spectrum is visible. In (b), only the resonance positions are shown and for both centers the simulation (solid and dashed lines for AA-EPR I, respectively, AA-EPR II) includes the six possible pathways for the single-crystal resonance field positions. The dotted line and resonance positions marked with an arrow represent a forbidden $-3/2 \leftrightarrow 1/2$ transition of AA-EPR II on a *zy* oriented line.

commercial plate, demonstrating that essentially the same signal is found in both materials, which substantiates the relevance of the present work for the actual applications.

Varying both the experimental recording and sample conditions, we attempted to obtain additional information that would lead to a complete analysis of this complex *Q* band ⟨100⟩ spectrum.

(i) When the microwave power is varied, in order to separate the spectra of defects with different relaxation behavior, no relative intensity changes between the resonance lines in the ⟨100⟩ spectrum occur.

(ii) The *W* band ⟨100⟩ spectrum (see below) reveals several transitions which cannot be reached in the *Q* band setup. Since the complete spectrum consists of more than 14 line packets, the RT interpretation in terms of only one tetragonal center should be discarded.

(iii) When comparing the ⟨100⟩, the complete powder, and the 2D powder spectrum (see below), the same features occur at the same field positions. This indicates that the *g* and ZFS tensors in the spin Hamiltonian have their principal axes along or close to ⟨100⟩ orientations. The extra information obtained in this way appeared anyhow still insufficient for a complete analysis of the EPR spectrum.

B. Angular variation at 4 K in *Q* band

Making use of the specific orientation of the needles on the plate, an EPR angular variation provided the key to the spectrum analysis. When the magnetic field is rotated in a plane perpendicular to the plate, both the single-crystal-like ⟨100⟩ and the 2D powder spectrum can be recorded with a 90° interval. A resonance position in the ⟨100⟩ spectrum of a defect with its principal *z* axis oriented along the needle axes splits into maximum two visible lines when the magnetic field is rotated toward the plate plane, leading—after 90° rotation—to either one perpendicular or an *x* and *y* components in the 2D powder spectrum. From Fig. 2(a), it is clear that due to an enhanced broadening at larger angles, these

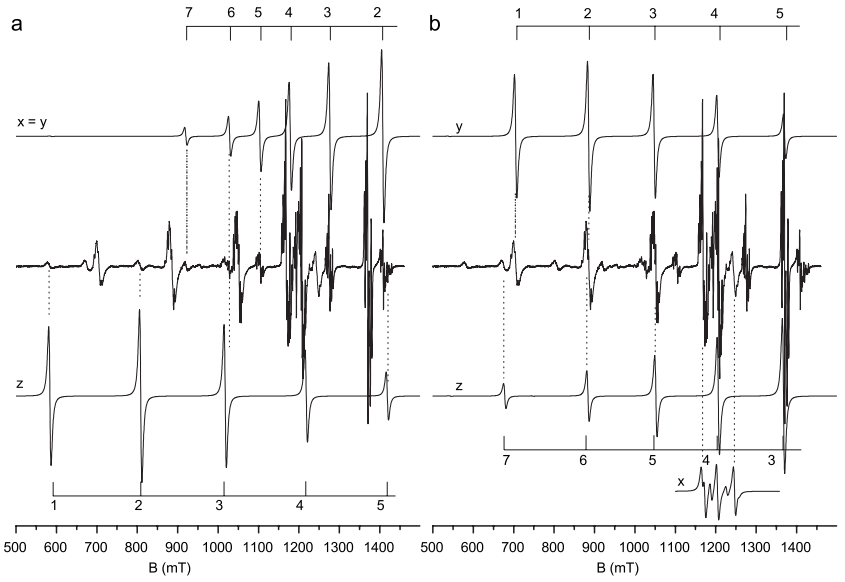

FIG. 3. Experimental and simulated 4 K *Q* band ⟨100⟩ spectrum of a $CsBr:Eu^{2+}$ NIP. On the simulations of (a) AA-EPR I and (b) AA-EPR II both the orientation as well as the transition is indicated: 1 represents the $-7/2 \leftrightarrow -5/2$ transition,…, 7 represents the $5/2 \leftrightarrow 7/2$ transition. The simulation parameters can be found in Table I; no SHF was included.

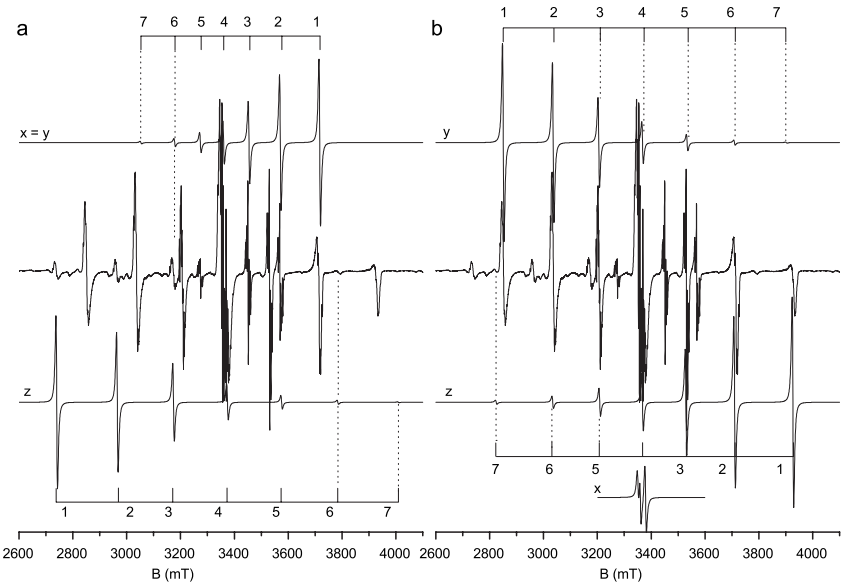

FIG. 4. Experimental and simulated 4 K *W* band ⟨100⟩ spectrum of a CsBr:Eu^{2+} NIP. On the simulations of (a) AA-EPR I and (b) AA-EPR II both the orientation as well as the transition is indicated: 1 represents the $-7/2 \leftrightarrow -5/2$ transition,…, 7 represents the $5/2 \leftrightarrow 7/2$ transition. The simulation parameters can be found in Table I; no SHF was included.

lines can only be easily followed close to the ⟨100⟩ orientation. Nevertheless, the angular variation was decisive in understanding the complex EPR spectrum. In Fig. 2(b), several branches exhibiting little anisotropy were found. These were attributed to the perpendicular component of a center with tetragonal symmetry, leading to the prediction of the other perpendicular and parallel components. As can be observed in Fig. 2(a), these transitions appear to belong to a minority species (labeled AA-EPR I). The remaining strong lines can all be attributed to a second center with orthorhombic symmetry (AA-EPR II), as clearly shown in Fig. 2(b) and further explained in Sec. III C. The spin Hamiltonian parameters determined from the angular variation were later optimized using the *Q* and *W* band spectra in the ⟨100⟩ orientation and can be found in Table I. The solid and dashed lines in Fig. 2(b), representing the simulations of AA-EPR I and II, respectively, as well as all other simulations in this work, were calculated using these parameters.

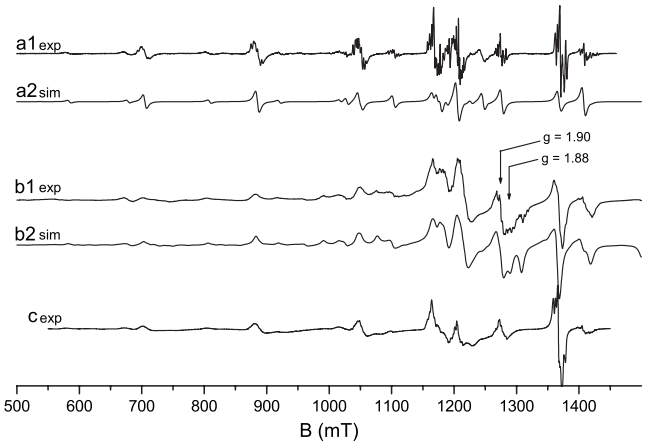

FIG. 5. 4 K *Q* band spectrum of a CsBr:Eu^{2+} NIP with the magnetic field perpendicular to the plate [(a) ⟨100⟩ spectrum], of a powdered NIP [(b) complete powder spectrum] and of a NIP with the magnetic field parallel to the plate [(c) 2D powder spectrum]. An optimized sum of the simulations of both AA-EPR I and II has been used (a2 and b2) to reproduce the experimental (a1 and b1) spectra. With arrows, the resonance fields belonging to two effective *g* values (see text) have been indicated.

C. Analysis of the two Eu^{2+} spectra at 4K

The AA-EPR I center has the same tetragonal symmetry as the earlier reported[4] AA-EPR center present at RT. The fourfold axis along a ⟨100⟩ orientation results in two different contributions to the ⟨100⟩ spectrum: both the perpendicular ($x=y$) and the parallel (z) orientations of the center are visible. The spectrum is, except for SHF structure, perfectly reproduced with the use of only three ZFS parameters $\mathbf{B}_2^0$, $\mathbf{B}_4^0$, and $\mathbf{B}_4^4$. Within the experimental error, the defect has an isotropic *g* tensor, as can be expected for an *S* state ion (Table I). The ⟨100⟩ simulation of AA-EPR I can be found in Figs. 3(a) and 4(a), where both the orientation and the $\mathbf{M_S} \leftrightarrow \mathbf{M_S}+1$ transition are indicated. "1" symbolizes the $-7/2 \leftrightarrow -5/2$ transition, "2" the $-5/2 \leftrightarrow -3/2$, etc., up to "7" for the $5/2 \leftrightarrow 7/2$ transition. Because of the low temperature, the absolute signs of the ZFS parameters could be determined from the population differences of the energy levels. This is particularly clear in *W* band [Fig. 3(a)], where certain simulated and experimental resonance lines have very low intensities, since the microwave quantum corresponds to 4.5 K.

For the simulation of the AA-EPR II spectrum, which dominates the 4 K spectrum, two more ZFS parameters are necessary, reflecting its orthorhombic II symmetry (all principal axes along ⟨100⟩ directions). Three orientations (x, y, and z) of the defect are represented in the ⟨100⟩ spectrum [Figs. 3(b) and 4(b)]. In Table I one can find that $\mathbf{B}_2^0 \approx \mathbf{B}_2^2$ implying that the center has nearly extreme rhombic symmetry better known under the condition $\mathbf{E}/\mathbf{D}=1/3$ ($\mathbf{D}=\mathbf{B}_2^0$ and $3\mathbf{E}=\mathbf{B}_2^2$). Extreme rhombic symmetry has earlier been found and discussed for several defects in various lattices.[9,10] When higher-order ZFS parameters are neglected, this special ratio for the ZFS parameters creates an identical ZFS in two main orientations (y and z), whereas in the third main orientation (x) the ZFS reduces to zero.

D. Reproduction of the ⟨100⟩ and powder spectra

In Fig. 5(a) the experimental ⟨100⟩ spectrum in *Q* band is shown together with an optimized sum of the simulations of the AA-EPR I and AA-EPR II spectra. This figure shows that while the resonance positions are reproduced perfectly, the intensities are not. This can in part be explained by the absence of SHF interactions in the simulations; but a similar problem occurred for the RT spectrum[4] where no SHF structure is resolved in the experimental spectrum. Other explanations involve strain in the ZFS parameters or the polymorphous seeding layer of the NIP, leading to a small powderlike component underlying the ⟨100⟩ spectrum.

In Fig. 5(b) the corresponding spectra are shown for a powdered NIP. Taken again into account that in the simulations no SHF interaction was included, there is a convincing correspondence between experiment and the simulations for AA-EPR I and AA-EPR II.

The 2D powder spectrum, i.e., the spectrum recorded when the magnetic field is parallel to the plate, in Figure 5(c), shows the same features that occur in the ⟨100⟩ and complete powder spectrum.

Q band EPR spectra at 10 K on CsBr:Eu NIPs produced by Fuji Photo Film Co., LTD were published before by Komiyama *et al.*[11] They reported spectra similar to our LT powder spectra, albeit with less structure, and found a difference in the resistance to x-ray damaging for two features appearing at effective *g* values of 1.90 and 1.88. The corresponding resonance fields were calculated and marked with an arrow in Fig. 5. When simulating the powder spectra of AA-EPR I and II using the values in Table I, one can derive that the effective *g* value of 1.90, respectively, 1.88 points to a feature present in the powder spectrum of AA-EPR I, respectively, AA-EPR II. So it seems very likely that Komiyama *et al.* referred to these two centers, although they did not report any further spectrum analysis. As a final test, we also investigated the resistance of the AA-EPR I and II centers to radiation damage. X-ray irradiation (both at RT and at LT) reduced the overall intensity of the EPR spectrum at LT. After LT irradiation, significant changes in the relative intensities of the two centers were found, while this was not the case after RT irradiation and subsequent cooling to the measuring temperature. AA-EPR II turned out to have a higher resistance to LT irradiation than AA-EPR I, in disagreement with the findings of Komiyama *et al.*

E. Temperature dependence of the ⟨100⟩ spectrum in *Q* band

To make the link between the RT (one tetragonal center) and the 4 K (one tetragonal and one orthorhombic center) spectra, the ⟨100⟩ spectrum was recorded at various temperatures as shown in Fig. 6. As the spectra were collected from experiments on several days and as sample positioning has an effect on the EPR intensity, the differences in signal-to-noise ratio are not believed to be relevant. The $x=y$ (perpendicular) and z (parallel) components are indicated in the RT spectrum.

From RT down to about 40 K, the AA-EPR spectrum can be followed, albeit with temperature-dependent $\mathbf{B}_2^0$, $\mathbf{B}_4^0$, and $\mathbf{B}_4^4$ parameters. It should, however, be noted that only the parallel component can be clearly followed in this temperature range, whereas the perpendicular component broadens and eventually seems to disappear at lower temperatures. Around 35 K, the spectrum gradually undergoes a more drastic change by the appearance of extra lines and an interpretation in terms of a single center is no longer possible. From 15 K down to 4 K, SHF structure is increasingly better resolved and the spectrum contains the two components (AA-EPR I and II), as described above. In Fig. 7 the temperature behavior of $\mathbf{B}_2^0$—the ZFS parameter reflecting the main axial distortion of AA-EPR and AA-EPR I—is depicted. The absolute signs of the ZFS parameters of AA-EPR can, however, not be determined at higher temperatures and we have chosen them to match the sign of $\mathbf{B}_2^0$ for AA-EPR I. The temperature dependence of the other ZFS parameters is indebted with larger experimental errors and shows a less smooth behavior. At $T>40$ K, respectively, $T<25$ K $\mathbf{B}_2^0$ clearly ap-

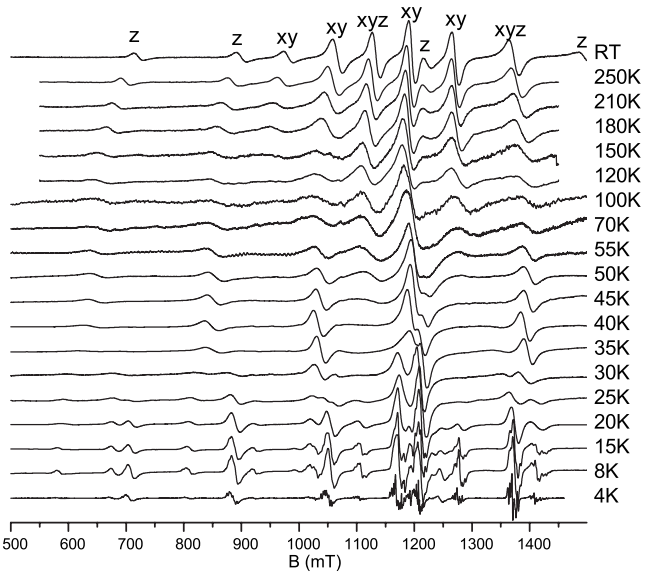

FIG. 6. Temperature scan of the ⟨100⟩ spectrum of a NIP at *Q* band. All EPR spectra have been recorded at optimal measuring conditions.

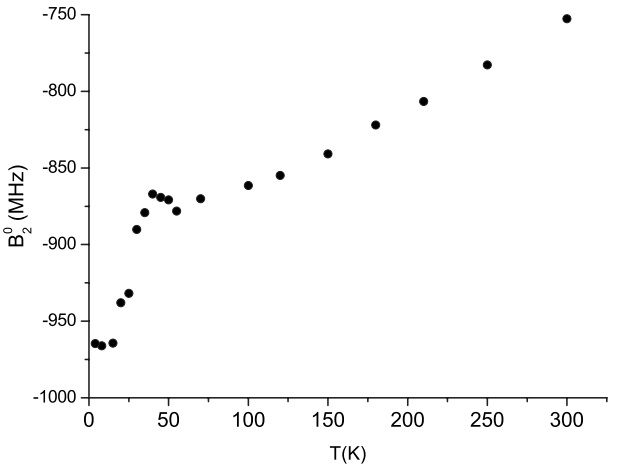

FIG. 7. Temperature dependence of the $\mathbf{B}_2^0$ parameter of AA-EPR (35 K–RT) and AA-EPR I (4 K–35 K).

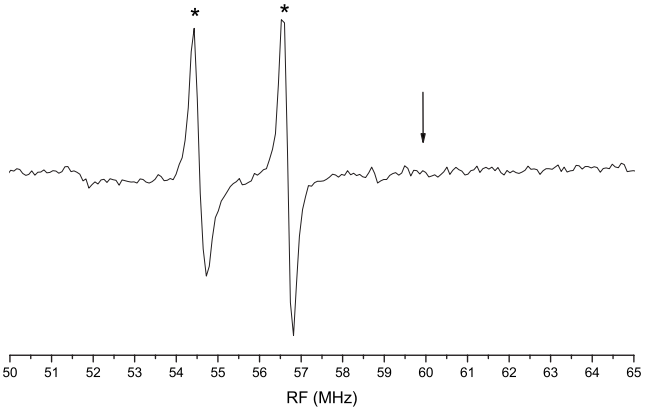

FIG. 8. ENDOR spectrum at 4 K of AA-EPR I at $B=1407$ mT (M_S: $-5/2 \leftrightarrow 3/2$ transition, at the $x=y$ orientation). The arrow indicates the ^{1}H-Larmor frequency and the asterisks show the ^{1}H interactions.

plies to AA-EPR, respectively, AA-EPR I. The fundamental changes in the spectra around 35 K are also reflected in the behavior of the $\mathbf{B}_2^0$ parameter and in this temperature region it is not possible to assign $\mathbf{B}_2^0$ unambiguously to either one of the tetragonal defects.

F. Preliminary ENDOR measurements

Only at very low temperatures ($T<4$ K) ENDOR can be detected for both AA-EPR I and AA-EPR II centers. Although the complete analysis is quite complex and still ongoing, preliminary work shows that several intense transitions can be attributed to ^{1}H nuclei based on their spectral position and shift as a function of magnetic field. In Fig. 8, an ENDOR spectrum recorded at one of the AA-EPR I transitions is shown where the ^{1}H Larmor frequency (arrow) and the transitions attributed to ^{1}H (asterisks) are indicated. Because the EPR line corresponds to a M_S: $-5/2 \leftrightarrow -3/2$ transition, both ENDOR lines are found on the same side of the ^{1}H Larmor frequency.

IV. DISCUSSION

Understanding the precise relationship and possible transformations between the three aforementioned spectra/defects (AA-EPR, AA-EPR I, and AA-EPR II) implies their identification and thus the investigation of plausible defect models. As will be argued below, there is little doubt that the core of the three defects is Eu^{2+}, in spite of the differences between them. Moreover, the temperature dependence of the spectra suggests a common basic structure for the three centers.

A. Identification as Eu^{2+}

EPR literature about Eu^{2+} in cesium halides and in CsBr, in particular, is scarce, at variance with the abundance of results reported for the alkali halides with the NaCl structure.[12–15] Only Savelev *et al.*[16] reported a Eu^{2+} center in CsBr single crystals obtained by (vacuum) heating at 500 °C and subsequent quenching. This center has been attributed to a Eu^{2+}-V_{Cs^+} dipole and its instability at RT was explained by

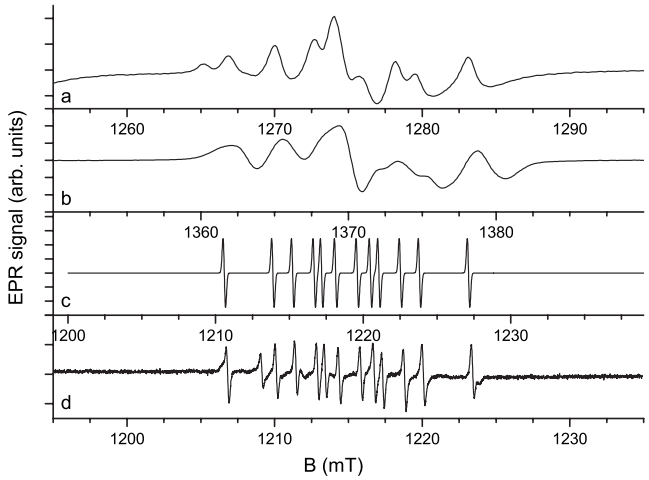

FIG. 9. Various Q band spectra. A part of the 4 K ⟨100⟩ spectrum of a NIP belonging to, respectively, (a) AA-EPR I and (b) AA-EPR II is compared with (c) a simulation of a ^{151}Eu/^{153}Eu hyperfine packet [with $^{151}A=-92.3$ MHz (Ref. 13)] and (d) the 20 K EPR spectrum of a 500 °C vacuum annealed powdered NIP.

the aggregation of these dipoles. In spite of the absence of spectra and spin-Hamiltonian parameters in his report (mainly focusing on decay kinetics), we were very likely able to detect the same spectra both in NIP samples and in Bridgman single crystals, but only after heating the samples in vacuum at 500 °C. As a result of this heat treatment, the AA-EPR-type spectra irreversibly disappear. Also in the NaCl-type alkali halides, the dominant Eu^{2+} centers have been identified as Eu^{2+}-V_{A^+}, more specifically with the vacancy in a nearest-neighbor (NN) position, leading to defects with orthorhombic I symmetry (principal axes along ⟨110⟩, $\langle 1\bar{1}0\rangle$, and ⟨001⟩). These dipoles furthermore show an aggregation behavior,[17] although much slower than reported in CsBr.[16]

Identification of Eu^{2+} centers may be based on their HF structure, as it shows little dependence on the ligand structure.[12–15,18–20] In Fig. 9 the LT spectrum is zoomed in on two SHF split transitions that show no overlap with other transitions. For comparison, the HF structure of the spectrum produced in powdered NIPs by vacuum annealing to 500 °C is also shown, along with a simulation of the expected $^{151/153}$Eu HF structure for a typical $A(^{151}\mathrm{Eu})$ of −92.3 MHz (Eu^{2+} in NaBr, Ref. 13). In both types of spectra, essentially the same components are present, although the width of individual HF lines in the AA-EPR I/II spectra is substantially larger than in the lower spectra. On the one hand this strongly suggests that the core of the AA-EPR type centers consists of one Eu^{2+} ion and effectively rules out Eu^{2+} aggregate centers as a model. On the other hand, the larger linewidth points to an increased interaction with neighboring nuclei (e.g., with ^{1}H nuclei). In the remainder of this section, we will discuss the validity of microscopic models for the paramagnetic centers under study here. As no complete ENDOR data are available yet, these models are inspired by the literature of Eu^{2+} in alkali halides and divalent transition-metal ion complexes in CsCl-type lattices.

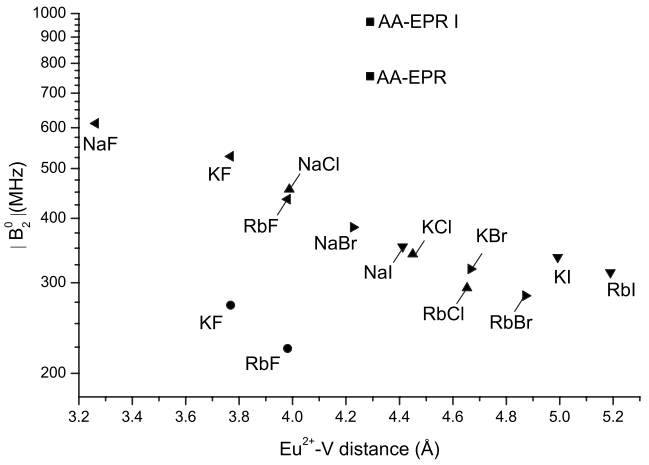

FIG. 10. $|\mathbf{B}_2^0|$ parameter of the Eu^{2+}-vacancy dipole as a function of the Eu^{2+}-vacancy distance in various systems. Data from Ref. 12 (▲), Ref. 13 (▶), Ref. 14 (▼), Ref. 15 (◀), Ref. 21 (●), and Table I (■). For AA-EPR and AA-EPR I, the values were taken at RT, respectively, 4 K.

B. Eu^{2+}-nV_{Cs^+} models

Based on the earlier work on alkali halides, one might be tempted to propose models solely consisting of Eu^{2+} and neighboring Cs^+ vacancies (V) for the three AA-EPR type centers encountered. Vacancies are expected to compensate the extra positive charge introduced in the lattice by a Eu^{2+} ion that is replacing a Cs^+ or is taking an interstitial position. They may also accommodate the stress induced in the lattice by the incorporation of the impurity. Assuming that Eu^{2+} takes a substitutional position (i.e., replacing a Cs^+), one V in a NN position provides the right symmetry for the AA-EPR and AA-EPR I center. For AA-EPR II, at least two vacancies are necessary [in next-nearest neighbor (NNN) (1,1,0) and (1,−1,0) positions]. One may then think of temperature-induced motion of the vacancies around the complex to produce the temperature dependence of the EPR spectrum, as has, e.g., been suggested for Cr^{3+} complexes in alkali halides.[9] There are, however, important objections against such identifications, as explained below.

First, AA-EPR(I) has a much larger ZFS parameter than expected for a $Eu^{2+}_{Cs^+}$-V_{Cs^+} model based on comparison with the NaCl-type alkali halides. This is shown in Fig. 10 where literature data for $|\mathbf{B}_2^0|$ of these dipoles are plotted as a function of the Eu^{2+}-V distance, along with the corresponding data points for AA-EPR and AA-EPR I. Although it is not *a priori* clear that the Eu^{2+}-V distance is the only parameter determining the size of $\mathbf{B}_2^0$, this might be considered an indication of an important relaxation of the Eu^{2+} ion toward the vacancy—or that more vacancies are involved—although only one is sufficient for charge compensation. Two other Eu^{2+} signals with an unexpected $|\mathbf{B}_2^0|$ result from the work of Boldu *et al.*[21] on RbF and KF and do not match the results of Iwasaki *et al.*[15] on the same crystals. It is interesting to note that Boldu *et al.* reported in the same article three other Eu^{2+} sites in KF and one of them had a negative $\mathbf{B}_2^0$. At that time, it was the first time a negative sign was determined for the dominant $\mathbf{B}_2^0$ term of Eu^{2+} in an alkali halide crystal.

Considering the centers to have two vacancies (with both vacancies in NN positions or NNN positions [AA-EPR(I), respectively, AA-EPR II)] implies that a large number of other configurations would then in principle be possible as well [as, e.g., observed for Cr^{3+} in NaCl (Ref. 9)]. Considering three vacancies enables all vacancies to be present in NN positions but implies an overcompensation for the AA-EPR II center by two and seems not very plausible.

In addition, for all vacancy-related models, the temperature dependence of the spectra is difficult to explain. A temperature-driven reversible migration for some of the defects of both vacancies from NN to NNN positions (lowering T) in very specific configurations seems very unlikely. A reversible migration of vacancies away from (and back to when lowering T) a complex that is already electrically repelling them is also not obvious.

An even more important argument against simple Eu^{2+}-nV_{Cs^+} models for the AA-EPR type centers is that these centers cannot be produced in melt-grown single crystals. They cannot even be produced by heating the crystals in vacuum to temperatures close to the melting point and subsequent quench to, e.g., 77 K, although this operation is expected to disperse aggregated Eu^{2+} ions in the lattice and promote the creation of cation vacancies. On the contrary, the AA-EPR-type centers, which are solely produced in NIPs, are irreversibly destroyed by the treatment expected to promote the creation of Eu^{2+}-nV_{Cs^+} centers. It is furthermore worth noting that the center studied by Savelev *et al.*,[16] the spectrum of which is shown in Fig. 9(d) and strongly differs from all three spectra in focus here is produced in this way.

This brings us to the conclusion that a lattice defect, most probably of extrinsic nature and certainly related to the growth conditions of the NIPs, prevents (part of) the Eu^{2+} from aggregating and gives rise to the AA-EPR-type contributions in the EPR spectra. In Sec. IV C, the possible nature of this/these defect(s) is discussed.

C. Impurity-associated Eu^{2+} models

To our knowledge, there are no reports on impurity-associated Eu^{2+} centers in CsCl-type lattices. For the divalent Mn^{2+} and Cu^{2+} doped in NH_4X (X=Cl or Br), such literature does exist. In $NH_4Cl:Mn^{2+}$, two axial centers have been attributed to interstitially located Mn^{2+}, coplanar with four chlorine ions.[22] The difference between these centers is attributed to the "axial" ligands which were proposed to be two H_2O molecules in one case and one H_2O and one NH_4^+ in the other. Boettcher and Spaeth[23,24] combined ENDOR and EPR to investigate two centers in $NH_4Cl:Cu^{2+}$. They found that in both cases, the Cu^{2+} takes an interstitial position, in the center of four Cl^- ions, and is charge compensated by cation vacancies at the NN positions on the same ⟨100⟩ axis. In one of the centers, which changes its symmetry from tetragonal to orthorhombic I when cooling down below 20 K, the ion has H_2O as fifth and sixth ligands, taking these cation vacancy positions. The other center remained tetragonal down to 1.6 K and was identified as having NH_3 molecules as axial ligands. Similar models have also been proposed for Cr^{3+} centers in CsCl and NH_4Cl.[25]

In view of the growth conditions of the NIPs, NH_3 incorporation seems highly unlikely, but building in H_2O is certainly possible. Furthermore, postannealing treatments of the plates at 170–180 °C in wet air increase both the sensitivity and the AA-EPR intensity of the NIP.[6,26,27] Identification of the stabilizing impurity near Eu^{2+} as H_2O or a related molecular ion, e.g., OH^-, thus seems plausible. Our aforementioned ENDOR results seem to affirm this possibility.

The EPR spectrum of aqueous $CsBr:Mn^{2+}$ single crystals has been investigated by Iri and Kuwabara[28] and strikingly analogous results to our study were found. One center with tetragonal symmetry was observed at RT and its intensity was increased by a short anneal at 300 °C. This center was tentatively assigned to a Mn^{2+}-V_{Cs^+} dipole, but a large off-center displacement of the Mn^{2+} ion had to be considered to explain the extremely large value of $\mathbf{B}_2^0$ in comparison with those for NaCl-type alkali halides. In view of the growth from aqueous solution, in our opinion, a H_2O-associated interstitial Mn^{2+} ion is not far fetched as a model for this center. We have checked that exactly this center is produced in the NIPs when doping them with Mn^{2+}, instead of Eu^{2+}.

In view of similarities in the temperature-induced change in symmetry, the model for the H_2O-associated Cu^{2+} center in NH_4Cl, as determined by Böttcher and Spaeth,[23,24] deserves further attention. A thermally activated rotation of the H_2O molecule around its C_2 axis, parallel to the main symmetry axis of the complex—setting in above 20 K—is held responsible for the temperature behavior. An analogous model for the AA-EPR-type centers would consist of an interstitial Eu^{2+} ion, in the center of a plane of four Br^- ions, with two H_2O ligands along the axis perpendicular to that plane. When at high temperature the H_2O ligands rotate around their C_2 axis, an axial center is expected, conform observations (AA-EPR). In order for the model to explain the symmetry of the centers at $T<35$ K, this rotation should freeze out leaving the H_2O molecules in {100} planes, at variance with the situation in NH_4Cl. Moreover, for the minority AA-EPR I center, the H_2O planes would be perpendicular to each other (D_{2d} point group), whereas for AA-EPR II both H_2O molecules would lie in the same {100} plane (D_{2h} symmetry).

Although this model gives a qualitatively correct picture of the temperature-induced symmetry changes for the centers, its validity is less obvious if one regard the problem in a more quantitative way. Indeed, in all three models, the $(EuBr_4O_2)^{4-}$ core of the complex is expected to impose the main axial D_{4h} symmetry, while the (static/dynamic) arrangement of four protons induces a small perturbation that only in the case of the D_{2h} center lowers the symmetry observed in EPR experiments. Without additional experimental or theoretical support, it seems hard to imagine that this perturbation would provide an explanation for the difference between the AA-EPR I center with perfectly axial and the AA-EPR II with nearly extremely rhombic symmetry. A valid model explaining the experimentally observed temperature behavior in this way should—in our opinion—rather have a basic structure that is cubic, on which perturbing entities, most probably H_2O molecules, superimpose a weak axial or orthorhombic distortion. The ongoing ENDOR experiments and planned density-functional modeling will hopefully bring us a more complete picture of these defects, which apparently are crucial to the PSL process in the plates.[6] This information would then also lead to an understanding of the thermally induced changes in the EPR spectra and, among others, the connection between the three observed spectra, as this is not entirely clear from experiment at present.

V. CONCLUSION

Analysis of the LT ($T<30$ K) EPR spectrum of $CsBr:Eu^{2+}$ NIPs demonstrates that two Eu^{2+} related defects are present: a dominant center with orthorhombic II symmetry (AA-EPR II) and a tetragonal minority center (AA-EPR I). The spectrum undergoes drastic changes in the 30–40 K range and from 40 K on upward gradually evolves into the previously studied RT spectrum dominated by one type of tetragonal Eu^{2+} center (AA-EPR). At all temperatures, these stable EPR spectra of the NIPs are clearly different from the spectrum produced by heating CsBr:Eu NIPs or melt-grown single crystals to 500 °C and which decays at RT. Comparison with literature data for Eu^{2+} centers in NaCl-type crystals and divalent transition-metal ions in CsCl-type crystals leads us to conclude that in the AA-EPR type centers, Eu^{2+} is associated with an impurity related to the synthesis conditions of the NIPs and preventing aggregation.

ACKNOWLEDGMENTS

E. Sagstuen (University of Oslo) and H. De Cooman are gratefully acknowledged for measurements on NIPs after *in situ* irradiation at 10 K. This work was financially supported by the Flemish Research Foundation (FWO-Vlaanderen, Grant No. G.0116.06) and Agfa-Healthcare NV.

[1] J. A. Rowlands, Phys. Med. Biol. **47**, R123 (2002).
[2] P. Leblans, L. Struye, and P. Willems, J. Digit Imaging **13**, 117 (2000).
[3] S. Schweizer, Phys. Status Solidi A **187**, 335 (2001).
[4] F. Loncke, H. Vrielinck, P. Matthys, F. Callens, J.-P. Tahon, and P. Leblans, Spectrochim. Acta, Part A **69**, 1322 (2008).
[5] S. Schweizer, U. Rogulis, S. Assman, and J.-M. Spaeth, Radiat. Meas. **33**, 483 (2001).
[6] F. Loncke, H. Vrielinck, P. Matthys, F. Callens, J.-P. Tahon, and P. Leblans, Appl. Phys. Lett. **92**, 204102 (2008).
[7] S. Stoll and A. Schweiger, J. Magn. Reson. **178**, 42 (2006).
[8] C. Rudowicz, J. Phys.: Condens. Matter **12**, L417 (2000).
[9] D. M. Wang and E. de Boer, Phys. Rev. B **39**, 11272 (1989).
[10] D. M. Wang and G. R. Hanson, J. Magn. Reson., Ser. A **118**, 1 (1996).
[11] T. Komiyama, M. Murofushi, and K. Takahashi, US Patent No.

2007/0075282 A1 (2006).
[12] G. S. Aguilar, E. P. Muñoz, H. S. Murietta, L. A. Boatner, and R. W. Reynolds, J. Chem. Phys. **60**, 4665 (1974).
[13] G. S. Aguilar, H. S. Murietta, J. O. Rubio, and E. P. Muñoz, J. Chem. Phys. **62**, 1197 (1975).
[14] J. O. Rubio, H. S. Murietta, E. P. Muñoz, J. O. Boldu, and G. S. Aguilar, J. Chem. Phys. **63**, 4222 (1975).
[15] T. Iwasaki, Y. Nakamura, and H. Wakabayashi, J. Phys. Soc. Jpn. **50**, 563 (1981).
[16] V. P. Savelev, V. P. Avdonin, L. D. Dugarova, A. P. Nedashkovskii, and B. T. Plachenov, Sov. Phys. Solid State **16**, 700 (1974).
[17] J. O. Rubio, J. Phys. Chem. Solids **52**, 101 (1991).
[18] M. A. Mondragon, R. J. Gleason, E. P. Muñoz, and J. L. Boldu, J. Chem. Phys. **89**, 7189 (1988).
[19] J. L. Boldu, R. J. Gleason, C. Quintanar, and E. P. Muñoz, J. Phys. Chem. Solids **57**, 267 (1996).
[20] S. Assman, S. Schweizer, and J. M. Spaeth, Phys. Status Solidi B **216**, 925 (1999).
[21] J. O. Boldu, E. P. Muñoz, W. K. Cory, and J. O. Rubio, J. Chem. Phys. **67**, 2391 (1977).
[22] S. Y. Chou and J. T. Yu, Chin. J. Phys. (Taipei) **29**, (pt. 3) 253 (1991).
[23] F. Boettcher and J. M. Spaeth, Phys. Status Solidi B **61**, 465 (1974).
[24] F. Boettcher and J. M. Spaeth, Phys. Status Solidi B **62**, 65 (1974).
[25] F. S. Stibbe and N. J. Trappeniers, Physica B & C **95**, 81 (1978).
[26] P. Hackenschmied, G. Schierning, M. Batentschuk, and A. Winnacker, J. Appl. Phys. **93**, 5109 (2003).
[27] M. Weidner, M. Batentschuk, F. Meister, A. Osvet, A. Winnacker, J.-P. Tahon, and P. Leblans, Radiat. Meas. **42**, 661 (2007).
[28] T. Iri and G. Kuwabara, J. Phys. Soc. Jpn. **23**, (pt. 3) 536 (1967).